

NeuroCSF: an fMRI method to measure contrast sensitivity function in human visual cortex

Laurie Goulet, and Reza Farivar

Department of Ophthalmology & Visual Sciences, McGill University, Montreal, Canada

Address correspondence to Reza Farivar. Email: reza.farivar@mcgill.ca

1 Abstract

2 The contrast sensitivity function (CSF) describes a range of spatial frequencies (SF) that
3 are detectable at a given level of contrast and is a very valuable tool both in clinical and
4 fundamental research. However, despite its immense value, the full potential of the CSF has not
5 been utilized in every aspect of clinical research due to time limits and patient factors. We propose
6 neuroCSF as a new method for measuring the CSF across the visual field directly from brain
7 activity, and with minimal demand from participants. NeuroCSF is a computational model that
8 estimates voxel-wise CSF parameters (i.e., peak contrast sensitivity, peak spatial frequency, and
9 spatial frequency bandwidth) from functional magnetic resonance imaging (fMRI) signals, under
10 controlled visual stimulation conditions. The approach extends the population spatial frequency
11 tuning (Aghajari, Vinke, & Ling, 2020) and population receptive field (Dumoulin & Wandell,
12 2008) methods to provide the first characterization of a full CSF using neuroimaging. We observe
13 that across early visual areas (V1, V2 and V3), the CSF peak spatial frequency and spatial
14 frequency cutoff are significantly higher for foveal eccentricity and decrease at parafoveal
15 eccentricities. Conversely, SF bandwidth slowly increases with eccentricity, while peak contrast
16 sensitivity remains constant with eccentricity for all early visual areas. Thus, cortical CSF
17 estimates vary systematically with eccentricity. The neuroCSF approach opens new perspectives
18 for the study of cortical visual functions in various disorders where the CSF is impacted, such as
19 amblyopia, traumatic brain injury, and multiple sclerosis.

20 Keywords

21 Contrast sensitivity function, visual field, fMRI, model-driven approach, visual perception

22 1. Introduction

23 The Contrast Sensitivity Function (CSF), originally developed by Campbell and Robson
24 (1968) describes the range of spatial frequencies detectable at varying levels of contrast. It is

25 widely acknowledged as the gold standard for evaluating visual performance. The CSF not only
26 serves to delineate the boundary between perceptually visible and invisible stimuli but also sheds
27 light on the limiting factors affecting everyday functional vision (Gervais, Harvey, & Roberts,
28 1984; Vision, 1985).

29 The CSF predicts visual target recognition in everyday life, encompassing tasks such as
30 recognizing faces (Owsley & Sloane, 1987; Stalin & Dalton, 2020; West et al., 2002), interpreting
31 road signs (Owsley & Sloane, 1987), deciphering letters, and performing real-world visual tasks
32 like reading, driving, and mobility (Legge, Rubin, Pelli, & Schleske, 1985; Lovie-Kitchin,
33 Mainstone, Robinson, & Brown, 1990; Marron & Bailey, 1982; Woods & Wood, 1995). Its ability
34 to assess the visual system's sensitivity to different levels of contrast provides crucial information
35 about the overall health and functioning of the system. In clinical visual sciences (Arden, 1978),
36 the CSF holds a vital place, serving as a non-invasive assessment tool for the detection and tracking
37 of visual impairments originating from ocular diseases or neurological deficits. Below, we briefly
38 discuss the clinical concerns for which CSF can be valuable (amblyopia, age-related macular
39 degeneration, and multiple sclerosis) and speculate on a fourth—post-concussive visual blur.

40 Amblyopia, commonly known as “lazy eye”, is characterized by reduced visual acuity in
41 an otherwise healthy eye and is often resulting from abnormal visual experience in early childhood.
42 It is traditionally diagnosed with visual acuity tests, but losses in contrast sensitivity have been
43 detected in amblyopes with reported normal visual acuity (Jindra & Zemon, 1989). Studies report
44 significant contrast sensitivity reductions in both the treated amblyopic eye (AE) and fellow-fixing
45 eye (FE) of "cured" amblyopic subjects when compared to control subjects (Cascairo, Mazow,
46 Holladay, & Prager, 1997; Chatzistefanou et al., 2005; Huang, Tao, Zhou, & Lu, 2007; Rogers,
47 Bremer, & Leguire, 1987; Sjöstrand, 1981; Wang, Zhao, Ding, & Wang, 2017). Analyzing the

48 CSF could thus aid in the detection and monitoring of amblyopia, providing insights into visual
49 symptoms that go beyond acuity measurements.

50 Age-related macular degeneration (AMD) is a progressive retinal disease that primarily
51 affects the central portion of the retina that is responsible for detailed vision. It is one of the leading
52 causes of vision impairments in the elderly (Wong et al., 2014). Early changes of AMD are
53 predominantly morphological and often occur without noticeable or measurable vision loss
54 symptoms. Conventional clinical tests, such as visual acuity, often miss these early subtle changes,
55 limiting their clinical utility in early and intermediate stages of AMD (Cocce et al., 2018; Klein,
56 Wang, Klein, Moss, & Meuer, 1995; Owsley, Huisingsh, Clark, Jackson, & McGwin, 2016).
57 Measuring early functional changes in AMD poses significant challenges and the CSF could be
58 instrumental in tracking functional vision loss associated with AMD (Hoffmann, Rossouw,
59 Guichard, & Hatz, 2020). In its early stage, AMD results in a CSF that is similar in shape to the
60 normal population, but that is shifted along both axes (Chung & Legge, 2016; Kleiner, Enger,
61 Alexander, & Fine, 1988). As the disease progresses, the CSF can reveal specific patterns of
62 deficits within the visual field, allowing clinicians to tailor interventions and monitor their
63 effectiveness.

64 Multiple sclerosis (MS), a disorder involving demyelination of the central nervous system,
65 is commonly manifested early on by ocular symptoms. Findings suggest that MS involves contrast
66 sensitivity deficits that precede changes in visual acuity (Chen & Gordon, 2005; Jackson, Ong, &
67 Ripley, 2004; McDonald & Barnes, 1992). A recent study by Nunes, Monteiro, and Vaz Pato
68 (2014) revealed that in its early stages, MS can produce highly selective contrast sensitivity loss
69 for high spatial frequencies. As the disease progresses, greater losses are seen in the low-

70 frequencies band. By assessing the contrast sensitivity function, clinicians can identify early signs
71 of MS in patients and track the progression of the disease.

72 While CSF degradation has been often considered in light of optical or ocular losses, in at
73 least one case—post-traumatic visual blur—the eyes and the optics appear normal but patients
74 report persistent “blur” (Collins et al., 2016; Ripley & Politzer, 2010). Because this type of blur
75 cannot be readily explained by ocular or optical factors, it necessitates neurological measures of
76 the CSF, which currently do not exist.

77 The major problem faced is that despite its immense value, the full potential of the CSF
78 has not been utilized in every aspect of clinical research, due to several challenges associated with
79 standard psychophysical CSF techniques, including time constraints, patient-related issues, and
80 technique limitations.

81 One of the primary challenges comes from the substantial time required to perform a full
82 CSF assessment at one retinal location (typically foveal), ranging from 15 to 30 minutes per eye.
83 This duration that already poses as a challenge for healthy participants can become almost
84 impossible to perform for a patient that also suffers from attention and/or fixation problems, visual
85 discomfort, or mobility issues (Harvey, 1997; Kelly & Savoie, 1973). Behavioral CSF measures
86 are also affected by extraneous factors such as fatigue, compliance, attention (Abramov et al.,
87 1984; Bradley & Freeman, 1982), emotional arousal (Lee, Baek, Lu, & Mather, 2014) and
88 feedback adaptation(Abrahamyan, Silva, Dakin, Carandini, & Gardner, 2016).

89 Crucially, CSF measures are typically done at one retinal location—foveally. In certain
90 visual deficits like amblyopia or age-related macular degeneration, visual impairments vary *across*
91 the visual field (Katz, Levi, & Bedell, 1984; Midena & Pilotto, 2017; Thomas, 1978). Currently to
92 obtain information about such visual field distinctions, the CSF must be behaviorally tested at

93 multiple positions, which poses challenges for both healthy and clinical participants. This is why
94 the standard laboratory methods for measuring the CSF have not been used to their full potential
95 in clinical research.

96 In recent years, various alternative approaches to psychophysical CSF measurement have
97 been proposed, but often at the cost of efficiency or validity. For instance, Visual Evoked Potentials
98 (VEPs) offer objectivity but vary in sensitivity (Hemptinne, Liu-Shuang, Yuksel, & Rossion, 2018;
99 Howe & Mitchell, 1984; Lopes de Faria, Katsumi, Arai, & Hirose, 1998). Similarly, methods
100 relying on eye movements, such as Gradiate (Mooney, Alam, Hill, & Prusky, 2020) or optokinetic
101 nystagmus (OKN) (Dakin & Turnbull, 2016; Jones, Kalwarowsky, Atkinson, Braddick, & Nardini,
102 2014), are reliable approaches that can be used with children or individuals with cognitive deficits,
103 but vary in complexity and efficacy, and fail to account for retinal location differences.

104 The CSF is a promising tool that can quantify subtle patterns of visual deficits that may
105 otherwise go unrecognized by current testing methods and provides information relevant for
106 disease progression and monitoring of treatment efficacy. Existing tools have a number of
107 constraints, mainly demanding extensive behavioural compliance and limited assessment at
108 multiple retinal locations. We sought to overcome these challenges to develop an objective
109 measure of the CSF across the visual field with minimal behavioural demands on the patient.

110 We have developed the neuroCSF, a method for directly estimating the CSF across the
111 visual field from functional Magnetic Resonance Imaging (fMRI) signals. The neuroCSF
112 objectively estimates voxel-wise CSF parameters, including peak contrast sensitivity, peak spatial
113 frequency, and spatial frequency bandwidth. This estimation process relies on a modeling
114 approach that translates the behavioral CSF model into a neural one.

115 The neuroCSF offers a substantial advantage over traditional approaches by
116 simultaneously measuring all visual field locations within an eccentricity limit in under 35 minutes
117 of scan time (and potentially much shorter, with further optimizations). It provides unbiased
118 measures of the CSF for each voxel across the visual brain without requiring input from
119 participants. This transformative method represents a significant advancement in CSF
120 measurement, offering an objective, fixation-independent, and non-invasive method to
121 simultaneously assess the entire visual field.

122 2. Materials and Methods

123 2.1. Subjects

124 Eight subjects with normal or corrected-to-normal vision (3 males; mean age, 27; range,
125 22-32 years) were recruited for this experiment. The participants had no prior history of binocular
126 dysfunction. Informed consent was obtained from each subject in accordance with the Code of
127 Ethics of the World Medical Association (Declaration of Helsinki) and was approved by the
128 Research Ethics Board of the McGill University Health Center.

129 2.2. Imaging

130 2.2.1. Display

131 Stimuli were generated using Psychtoolbox (Brainard, 1997) through MATLAB (2019a,
132 The Math Works Inc., Natick, Massachusetts) and displayed on a gamma-corrected 32" LCD
133 **BOLDScreen (Cambridge Research Systems)** at 120Hz with a mean luminance of 120 cd/m²
134 reflected by a mirror above the participant's head. Participants were placed at a viewing distance
135 of 152 cm from the monitor spanning 25.8 by 14.7 degrees of visual angle at a pixel resolution of
136 1920 by 1080. All stimuli were viewed binocularly.

137 **2.2.2. Equipment/setup**

138 Acquisition was performed on a Siemens Prisma 3T MRI Scanner at the Montreal General
139 Hospital (McGill University Health Center). Functional images were acquired using a 32-channel
140 vision coil (Farivar, Grigorov, van der Kouwe, Wald, & Keil, 2016) in a transverse plane
141 perpendicular to the calcarine sulcus with a standard simultaneous multislice (SMS) echo-planar
142 imaging (EPI) sequence (Resolution = 2 x 2 x 2 mm, TR= 1000ms, TE: 33ms, FA= 33°, fat
143 saturation, FOV = 128 x 128 mm, number of slices= 16, R=2, BW = 1698 Hz/pixel). Anatomical
144 images were obtained with a 64-channel head coil using a T1-weighted magnetization prepared-
145 rapid gradient echo (MPRAGE) sequence (Resolution = 0.8mm3, TR= 1780ms, TE=2.64ms, FA
146 = 90, FOV = 216 x 216 mm, number of slices= 208).

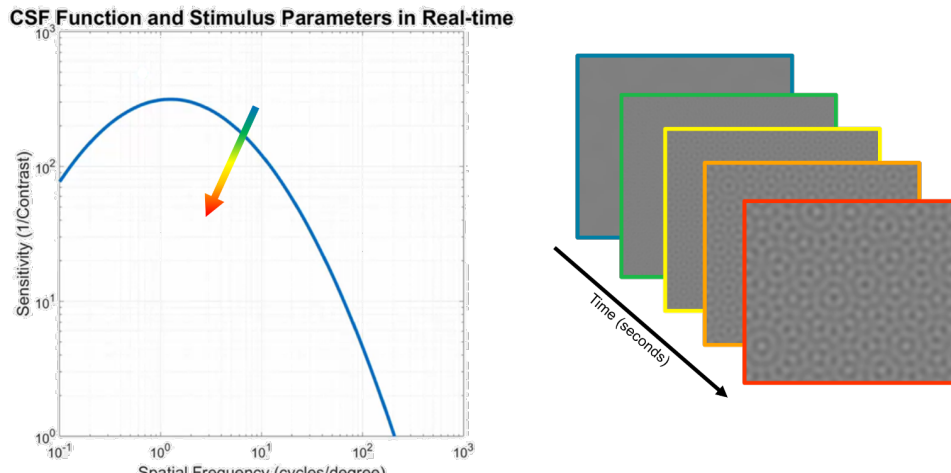
147 **2.2.3. Preprocessing of Functional Images**

148 Preprocessing of fMRI data was performed using Analysis of Functional NeuroImages
149 (AFNI) (Cox, 1996). To minimize spatial blurring, all spatial transformations following slice-time
150 correction (i.e., motion correction, distortion correction, registration to anatomical image) were
151 applied in a single step. Preprocessing of the T1-weighted anatomical images for alignment with
152 the functional images was performed using Freesurfer (<http://surfer.nmr.mgh.harvard.edu/>).

153 During the functional runs, we binocularly presented full-field stimuli that varied
154 systematically in contrast (min=10 % max=60%) and spatial frequency (min=0.033 cyc/° [cpd],
155 max=26cpd). Stimuli were generated by overlapping eight sinusoidal gratings with evenly spaced
156 rotations over 180°, making the stimuli not selective for any orientation.

157

2.3. NeuroCSF Stimuli & Experimental Procedure



158

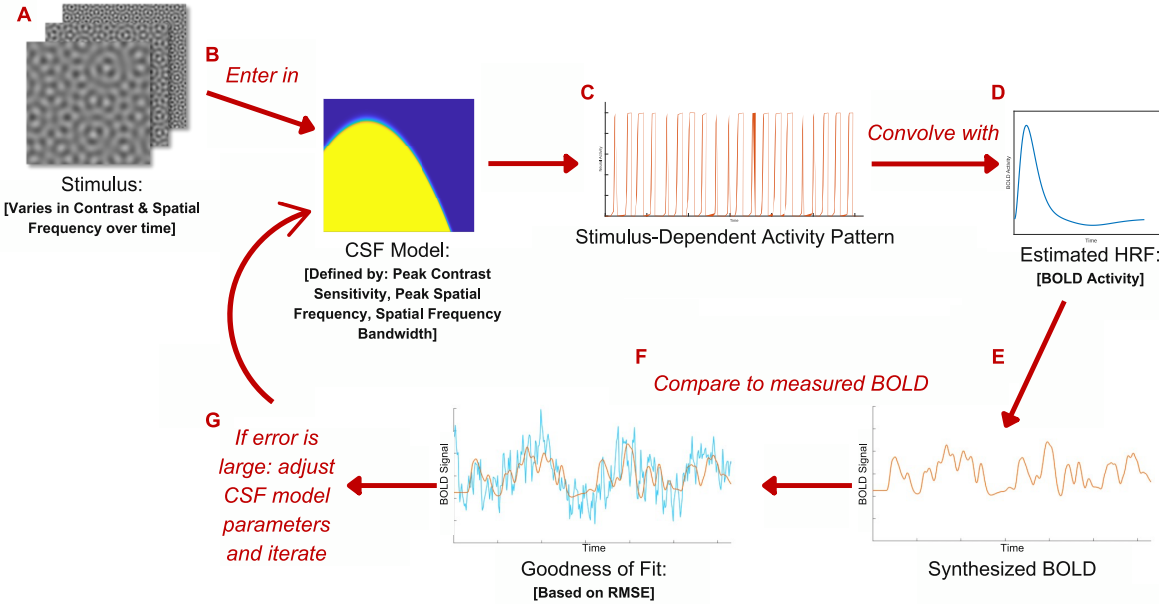
159 **Figure 1. Stimulus presentation sequence for the CSF modeling.** Depiction of one transition of the full field dynamic stimuli that
160 varies over time in spatial frequency and contrast (right). The five frames depicted are only a subset of the 300 frames that would
161 be presented within one of the 20 stimulus transitions. The stimulus consists of a contrast and spatial frequency vector (left) and
162 any of its time points represent a shift in this two-dimensional space of contrast and spatial frequency.

163 Each run included 20 ten-second periods of smoothly transitioning contrast-spatial
164 frequency vectors—crossing from the subthreshold to suprathreshold regimes of the CSF (Fig. 1)
165 —presented in a random sequence. The crossing points were evenly spaced (logarithmically)
166 across the expected range in the contrast-spatial frequency space. This smoothly dynamic stimuli
167 strategy ensured that we would capture activity, as measured through the blood oxygen level-
168 dependent (BOLD) response via fMRI, as it transitioned from zero response—when the stimulus
169 was subthreshold—to complete activation—when the stimulus was suprathreshold. We thus
170 captured the experience of an entire transition from subthreshold to suprathreshold and observed
171 the changes in neural activity as the brain began to detect the stimuli.

172 Each stimulus presentation was followed by a blank interstimulus interval defined by a
173 Gaussian distribution with a mean of 5s. To help with attention, participants were instructed to
174 report whenever they perceived the stimuli by pressing a key. Each session comprised of three

175 unique runs, with the same trajectories but shown in different orders, repeated twice, totaling
176 approximately 30 minutes.

177 **2.4. NeuroCSF Data Analysis**



178
179 **Figure 2. Depiction of the CSF model fitting method.** The procedure begins by assigning a canonical CSF to a voxel (B) and, in
180 consideration of the temporal profile of the stimulus (A), predicting the time-varying voxel response (C). This vector, convolved
181 with the hemodynamic response (D), yields a synthesized fMRI timeseries model (E), which can then be fitted to the measured fMRI
182 data from the voxel (F). If the fit does not sufficiently explain variability in the voxel's time series, we iterate until we converge on
183 a parameter set that best explains the voxel's response (G).

184 The different CSF transitions that we presented to the subjects during fMRI scan were
185 recorded along with the contrast, spatial frequency, and the precise transition time (Fig. 2A). The
186 challenge then becomes to identify the CSF model that, when taken into account to generate the
187 model hemodynamic response given the stimulation pattern, explains the bulk of the fMRI
188 response.

189 The CSF model was estimated by assigning an initial model of the CSF to each voxel,
190 defined by three parameters (i.e., peak contrast sensitivity, peak spatial frequency, spatial

191 frequency bandwidth) (Fig. 2B). The mathematical model of the CSF can be represented by a log-
192 parabola, $S'(f)$, defining sensitivity as (Watson & Ahumada, 2005):

193

194
$$S'(f) = \log_{10}(\gamma_{max}) - \kappa \left(\frac{\log_{10}(f) - \log_{10}(f_{max})}{\beta'/2} \right)^2. \quad (1)$$

195

196 Where $\kappa = \log_{10}(2)$, $\beta' = \log_{10}(2\beta)$, γ_{max} represents the peak sensitivity (1/Contrast),
197 f_{max} the peak spatial frequency in cycles per degree (cpd) and β the spatial frequency bandwidth
198 (octaves).

199 In this approach, the CSF model of each voxel was treated similarly to a receptive field
200 representing a boundary in log-log space of contrast sensitivity and spatial frequency. Any time-
201 point of our stimulus (Fig. 2A) represented a shift in this 2-D space of contrast and spatial
202 frequency, such that when the stimulus entered a voxel's receptive field or CSF boundary, and was
203 now suprathreshold, this would elicit a response from the voxel. By calculating the overlap
204 between the stimulus sequence (Fig. 2A) and the CSF model (Fig. 2B), we defined a time-varying
205 voxel response (Fig. 2C). The time-varying voxel response vector was then convolved with a
206 subject-specific and voxel-specific estimated hemodynamic response function (Fig. 2D) to
207 produce a synthesized BOLD timeseries. This produced a function that defined proportional
208 BOLD activity at every time point (Fig. 2E). This model BOLD time-series was then compared to
209 the measured BOLD time-series (Fig. 2F). The difference between the two was calculated using a
210 Goodness of Fit measurement (i.e., RMSE).

211 If the fit explained variability in the voxel sufficiently, the process stopped, and the
212 parameters of the initial CSF model were saved for that voxel. If not, we searched a parameter
213 space using a particle swarm optimization algorithm (Ab Wahab, Nefti-Meziani, & Atyabi, 2015;

214 Helwig, Branke, & Mostaghim, 2013; Mendes, Kennedy, & Neves, 2004) and iterated until we
215 converged on the set of CSF parameters that resulted in the best fit between the model and
216 measured BOLD timeseries (Fig. 2G). This process was repeated for every voxel in areas V1, V2,
217 and V3.

218 Based on the estimated CSF parameters (i.e., peak sensitivity, peak spatial frequency and
219 spatial frequency bandwidth), we then derived voxels' high spatial frequency cutoff from equation
220 1 by setting $S'(f)$ to 1 and then calculated the associated spatial frequency.

221 2.5. Hemodynamic Response Function (HRF) Estimation

222 Since the shape of the hemodynamic response function (HRF) can vary significantly
223 between people, we estimated individual HRF for each participant and modeled personalized HRF
224 for each voxel within our region of interest (ROI).

225 2.5.1. HRF-mapping stimulus

226 The stimulus consisted of a full field (radius 16° visual angle), high contrast texture,
227 consisting of a dynamic, high-contrast pseudo-checkerboard varying in spatial frequency and
228 phase function (Alvarez, De Haas, Clark, Rees, & Schwarzkopf, 2015), that briefly appeared on
229 the display for two seconds before returning to a static grey screen for a 20 second period. This
230 cycle was repeated 10 times, totalling one run of approximatively 5 minutes. Participants were
231 instructed to maintain their gaze on a central fixation point (size: 0.1 degree), and to report the
232 color change of the fixation dot.

233 2.5.2. HRF modelling

234 The HRF was fitted with the difference of two gamma density functions (Worsley et al.,
235 2002). The modeled parameters were the time-to-peak of the HRF response and HRF undershoot,

236 the full width at half maximum of the HRF response and HRF undershoot, the ratio adjusting the
237 amplitude of the HRF undershoot relative to the HRF response amplitude, and the scale factor for
238 the final HRF. The HRF parameters were optimized simultaneously using particle swarm non-
239 linear optimization algorithm.

240 2.6. Retinotopic Atlas ROIs

241 Surface location and retinotopy estimates (eccentricity and polar angle) of early visual
242 areas (V1,V2, and V3) were obtained by registering a probabilistic retinotopic atlas (N. C. Benson
243 et al., 2012) (https://cfn.upenn.edu/aguirre/wiki/doku.php?id=public:retinotopy_template) to each
244 subject's functional space.

245 2.7. NeuroCSF Voxel Selection

246 Only voxels with a receptive field center within the range of 0 to 6 degrees of eccentricity
247 were included in the analysis. We also only included gray matter voxels whose coefficient of
248 determination (R^2) was greater than the highest R^2 obtained in any white matter voxel (i.e., use the
249 distribution of R^2 in the white matter as a sample of trivial R^2 values). Based on this method, only
250 voxels with a minimum R^2 of 10% were included in the analysis.

251 2.8. Cross-validation

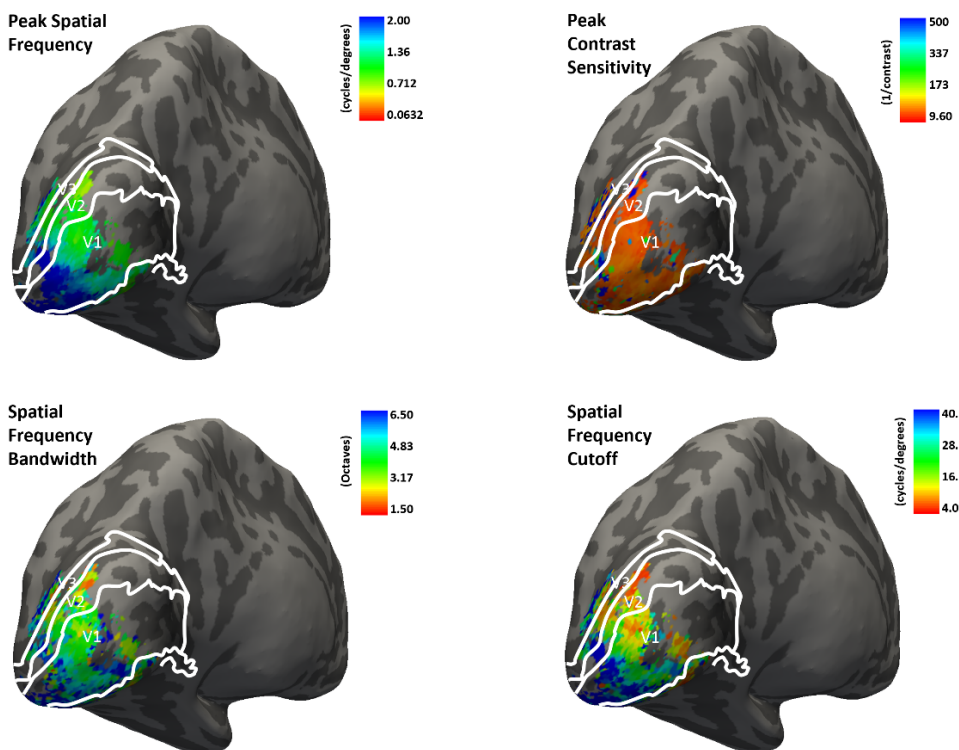
252 Each subject was observed with fMRI while viewing three unique runs of our novel
253 stimulus presentation. Each of these runs had a pair with perfectly matched presentation time, for
254 a total of 6 runs. To maximize the R^2 for the fit, we averaged the fMRI data from pairs of runs and
255 thus obtained three measurements of CSF parameters for each voxel. To validate the CSF
256 parameters, we employed leave-one-out-cross-validation (LOOCV) for each voxel in the early
257 visual cortex. Parameters from two pairs of runs were used to predict the time series of another

258 pair of runs, and an average CSF parameter set per voxel was calculated. Cutoff spatial frequency
259 was then derived for each voxel from equation 1.

260 **3. Results**

261 **3.1. Cortical CSF parameters consistency and eccentricity
262 variability in early visual areas**

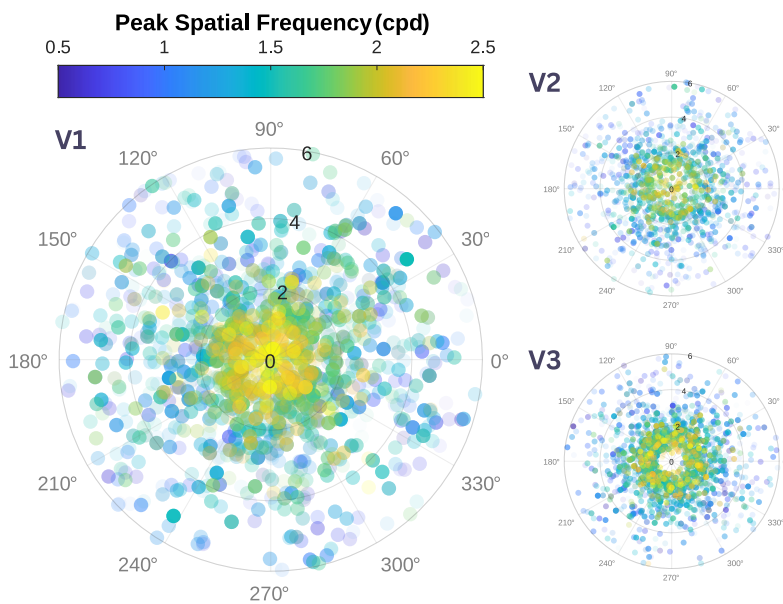
263 We first qualitatively assessed the organization of the CSF parameters across the
264 visuocortical map of early visual areas. Parameter estimates were projected onto the cortical
265 surface (Fig. 3) and the visual field maps (Fig. 4-7) to visualize local variations in CSF estimates
266 across the early visual areas and retinal location, respectively.



267
268 **Figure 3. Single subject CSF parameters estimate for subject S01.** Peak contrast sensitivity, peak spatial
269 frequency, spatial frequency bandwidth, and spatial frequency cutoff estimates from 0-6° eccentricity are plotted on the inflated hemisphere of a
270 single subject. Solid white lines indicate the borders between visual areas V1-V2-V3 obtained via N. C. Benson et al. (2012).

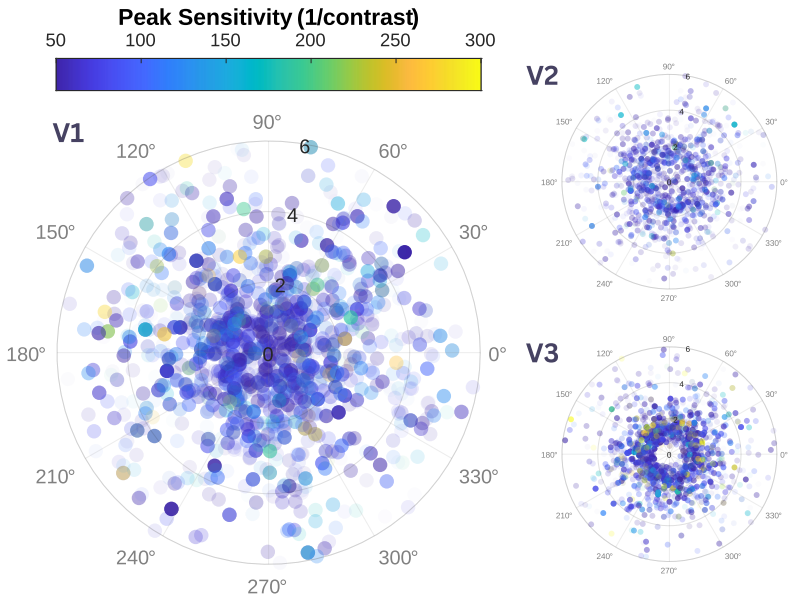
271 For all four parameters, the trends we observed were similar across early visual areas (Fig.
272 3). We observed systematic changes in peak spatial frequency selectivity with eccentricity. Figure

273 4 represents the magnitude of the voxel's peak spatial frequency across the visual field for areas
274 V1, V2, V3. Consistent with previous reports (Aghajari, Vinke, & Ling, 2020; Broderick,
275 Simoncelli, & Winawer, 2022; Henriksson, Nurminen, Hyvärinen, & Vanni, 2008; Hess, Li,
276 Mansouri, Thompson, & Hansen, 2009), voxels with foveal retinotopic preferences were selective
277 for higher spatial frequencies and this peak preference dropped as a function of eccentricity.



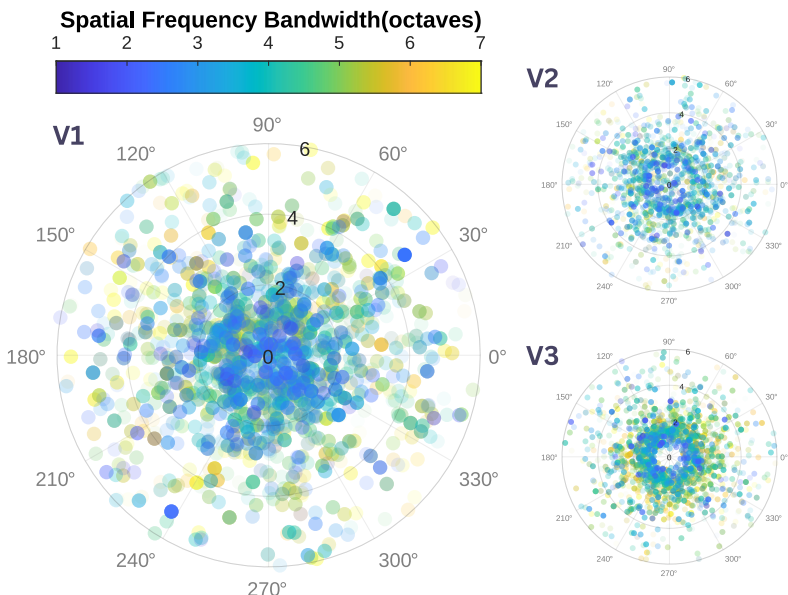
278
279 **Figure 4. Voxel-wise peak spatial frequency map across the visual field of early visual cortex.** Each circle represents a single
280 voxel. The magnitude of the voxel's peak spatial frequency in cycles per degree (cpd) is represented by a color code. Color
281 Transparency of the circles are scaled with their coefficient of determination (R^2) value for the neuroCSF fits. Their locations are
282 determined based on their polar angle and eccentricity coordinates. In all 3 visual areas (V1, V2, V3), peak spatial frequency is
283 higher for foveal eccentricity and decreases at parafoveal eccentricities.

284 Peak sensitivity values did not show significant shifts with eccentricity across all three
285 visual areas (Himmelberg, Winawer, & Carrasco, 2020; Rovamo, Franssila, & Näsänen, 1992;
286 Rovamo, Virsu, & NÄSÄNEN, 1978) (Fig. 5). This result aligns with previous studies, indicating
287 that our stimuli compensated for the reduced cortical representation of peripheral retinal
288 eccentricities (Himmelberg et al., 2020; Rovamo & Virsu, 1979; Rovamo et al., 1978; Virsu &
289 Rovamo, 1979).



290

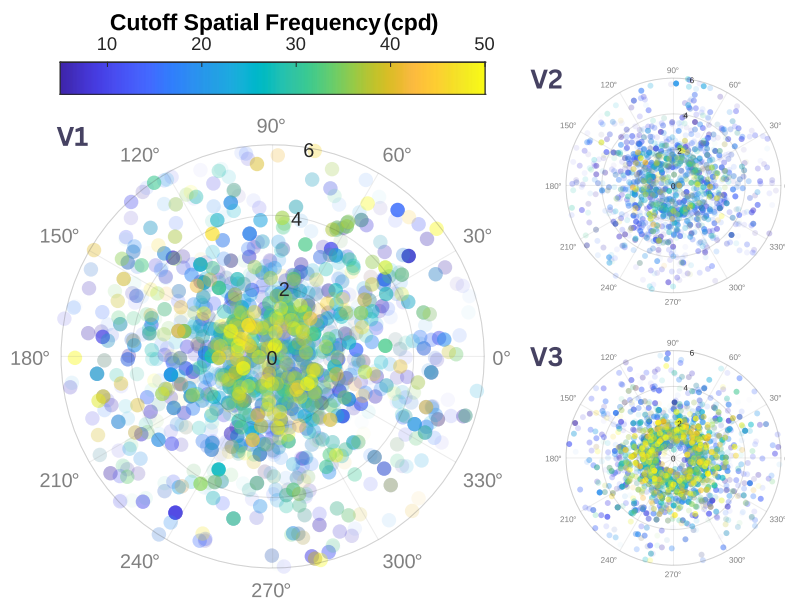
291 **Figure 5. Voxel-wise peak contrast sensitivity map across the visual field of early visual cortex.** Each circle represents a single
292 voxel. The magnitude of the voxel's peak sensitivity ($1/\text{contrast}$) is represented by a color code. Color Transparency of the circles
293 are scaled with their coefficient of determination (R^2) value for the neuroCSF fits. Their locations are determined based on their
294 polar angle and eccentricity coordinates. We can see that peak sensitivity values do not shift with eccentricity across all early
295 visual areas (V1, V2, V3).



296

297 **Figure 6. Voxel-wise spatial frequency bandwidth map across the visual field of early visual cortex.** Each circle represents a
298 single voxel. The magnitude of the voxel's spatial frequency bandwidth (octaves) is represented by a color code. Color
299 Transparency of the circles are scaled with their coefficient of determination (R^2) value for the neuroCSF fits. Their locations are
300 determined based on their polar angle and eccentricity coordinates. For area V1 and V2, foveal spatial frequency bandwidth is
301 narrower compared to the peripheral region. However, there is no clear trend for V3 voxels.

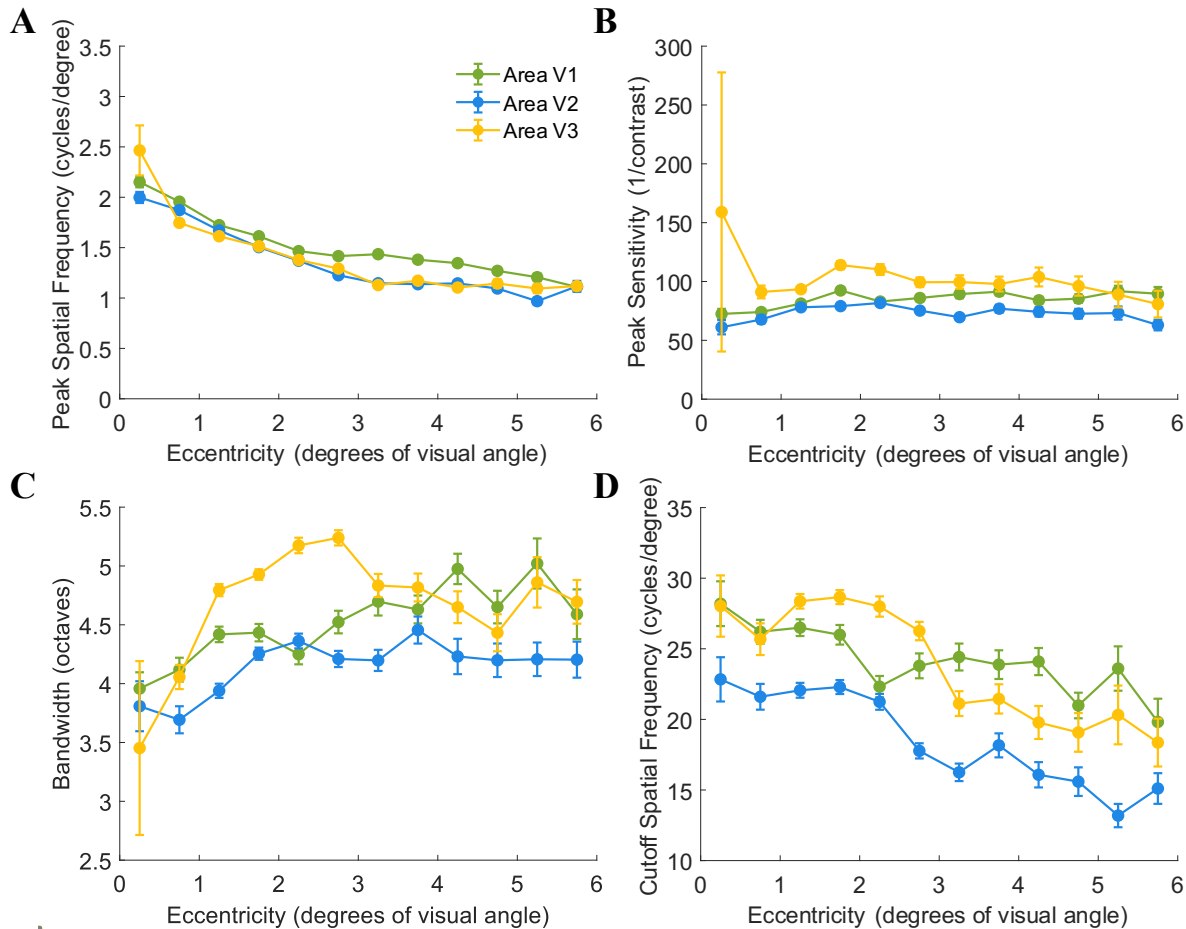
302 We observed a positive trend between spatial frequency bandwidth and retinal eccentricity
303 in V1 and V2 (Fig. 6). However, the relationship was not as clear for V3 voxels. Previous findings
304 from human and animal studies do not predict a clear relationship between spatial frequency
305 bandwidth and eccentricity. While Broderick et al. (2022); De Valois, Albrecht, and Thorell (1982)
306 found that bandwidth is mostly constant across eccentricity, Aghajari et al. (2020); Foster, Gaska,
307 Nagler, and Pollen (1985) only found a moderate increase in bandwidth with eccentricity. In both
308 cases, that increase was more pronounced in V1 compared to higher visual areas. Our results are
309 not inconsistent with those findings.



310
311 **Figure 7. Voxel-wise spatial frequency cutoff map across the visual field of early visual cortex.** Each circle represents a single
312 voxel. The magnitude of the voxel's spatial frequency cutoff (cpd) is represented by a color code. Color Transparency of the circles
313 are scaled with their coefficient of determination (R^2) value for the neuroCSF fits. Their locations are determined based on their
314 polar angle and eccentricity coordinates. We cannot see a clear trend between V1 voxels spatial frequency cutoff and eccentricity,
315 while spatial frequency cutoff values decrease with eccentricity across V2 and V3.

316 Spatial frequency cutoff showed a modest drop in parafoveal regions compared to foveal
317 regions, primarily in areas V2 and V3 (Fig. 7). High spatial frequency cutoffs remained mostly
318 constant across eccentricities for area V1.

319 To focus on the eccentricity-based effects, in the next analyses we collapsed our results
320 across polar angles, and we binned the data of our subject into 12 equal sized eccentricity bins
321 from zero to six degrees of visual angle (dva). We looked at the average parameter response as a
322 function of eccentricity and across early visual areas.



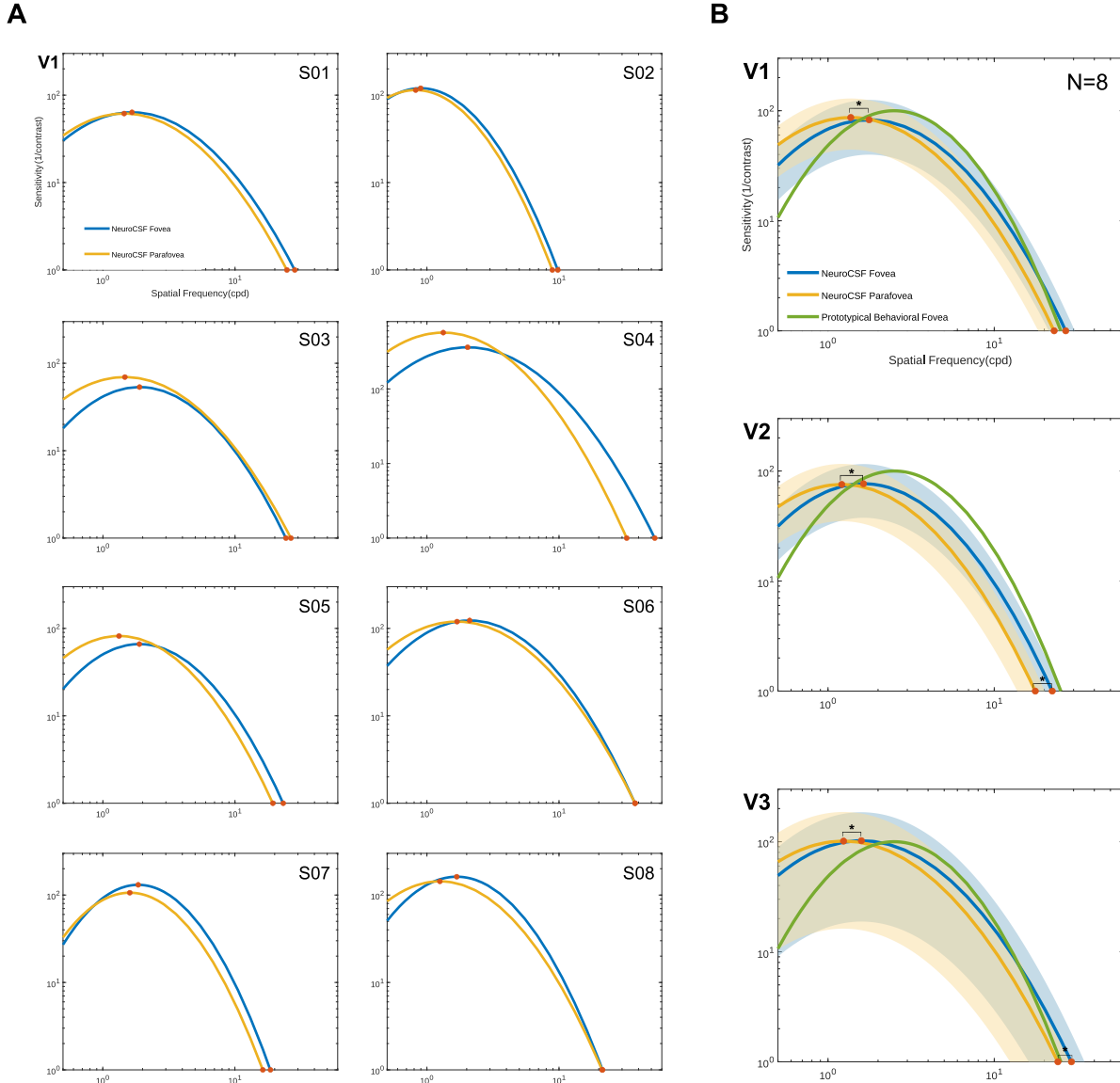
323 .
324 **Figure 8. Relationship between the CSF parameters and retinotopic eccentricity across early visual areas.** (A) Mean subject-
325 wise peak spatial frequency estimates within each eccentricity bin. Peak spatial frequency is higher for foveal eccentricity and
326 decreases at parafoveal eccentricities across V1-V2-V3. (B) Mean subject-wise peak sensitivity estimates within each eccentricity
327 bin. Peak gain is stable across eccentricity for all three visual areas. (C) Mean subject-wise spatial frequency bandwidth estimates
328 within each eccentricity bin. Spatial frequency bandwidth slightly increases with eccentricity in area V1 and V3. In area V2, spatial
329 frequency bandwidth is roughly stable across eccentricity. (D) Mean subject-wise spatial frequency cutoff estimates within each
330 eccentricity bin. In V1-V3, mean cutoff values are higher for the fovea compared to parafoveal eccentricities. 12 bins were linearly
331 spaced between the eccentricity range [0.25°, 5.75°]. Data from early visual areas (V1, V2, V3) is displayed by a different color.
332 Error bars show the mean \pm SE.

333 Previously observed trends were present across all CSF and visual areas (Fig. 8). We found
334 a negative relationship in V1-V3 when examining the average peak spatial frequency [V1: $r(12) =$

335 -0.926, P <0.001; V2: $r(12) = -0.820$ P <0.001; V3: $r(12) = -0.792$, P <0.001] and spatial frequency
336 cutoff [V1: $r(12) = -0.709$, P <0.01; V2: $r(12) = -0.666$, P <0.01; V3: $r(12) = -0.796$, P <0.001] as
337 a function of eccentricity across subjects, (Fig. 8a,d). We observed a positive trend between spatial
338 frequency bandwidth and retinal eccentricity but only for areas V1 and V2 [V1: $r(12) = 0.887$, P
339 <0.001; V2: $r(12) = 0.632$, P <0.05; V3: $r(12) = 0.475$, P = 0.086](Fig. 8c). Finally, our analysis
340 didn't reveal any association between peak contrast sensitivity and eccentricity [V1: $r(12) = 0.203$,
341 P = 0.486; V2: $r(12) = 0.177$, P = 0.545; V3: $r(12) = 0.326$, P = 0.256] (Fig. 8b).

342 We then calculated average parameters responses for foveal (i.e., 0-2 dva) and parafoveal
343 (i.e., 2-6 dva) eccentricities. With the help of equation 1, we defined CSF curves for foveal and
344 parafoveal eccentricities. Each panel of figure 9a displays two mean CSF curves, one for foveal
345 eccentricities and another for parafoveal eccentricities, for area V1-V2-V3 for all our subjects. We
346 then averaged these parameters to create averaged CSF curves across all our subjects and
347 performed a Wilcoxon Signed-Rank test (Fig. 9b). The prototypical behavioral CSF curve from
348 Lesmes, Lu, Baek, and Albright (2010) is also included as a reference.

349 The results show that there is a statistically significant difference in the mean response of
350 peak spatial frequency between foveal and parafoveal eccentricities in V1-V3 [V1: $Z = -2.660$, P
351 < 0.01; V2: $Z = -2.660$, P < 0.01; V3: $Z = -2.660$, P < 0.01], as well as spatial frequency cutoff
352 in V2-V3 [V1: $Z = -1.295$, P = 0.195; V2: $Z = -2.266$, P < 0.05; V3: $Z = -2.266$, P < 0.05].
353 However, there were no statistically significant differences in peak contrast sensitivity [V1: $Z = -$
354 0.069, P = 0.945; V2: $Z = -0.197$, P = 0.844; V3: $Z = -0.329$, P = 0.742] and spatial frequency
355 bandwidth [V1: $Z = 1.762$, P = 0.078; V2: $Z = 0.873$, P = 0.383; V3: $Z = 1.762$, P = 0.078]
356 between fovea and parafovea.



357

358 **Figure 9. Estimated CSFs across early visual areas.** (A) Estimated individualized CSFs across V1. Each panel displays one set of
359 estimated CSFs for area V1 of one of our 8 subjects. (B) Average \pm standard deviation of the CSF across areas V1, V2, and V3.
360 Data from foveal (0-2 dva) and parafoveal (2-6 dva) eccentricities is displayed by a different color, blue and yellow respectively.
361 The prototypical behavioral CSF curve from Lesmes et al. (2010) is also included in green as a reference. The shading represents
362 one standard deviation above and below the mean. Significant differences ($P < 0.05$) between neuroCSF fovea and parafovea are
363 indicated by (*).

364 3.2. Intraclass Correlation Coefficient (ICC) Analysis for 365 Reliability Assessment

366 In many settings, including clinical research, reducing the number of acquisitions can
367 significantly decrease participant burden, scanner time, and associated costs. We performed an
368 analysis to optimize future data collection, balancing reliability with time and cost efficiency. The

369 goal was to identify the minimal number of runs needed to maintain data quality equivalent to that
370 obtained with the maximal number of runs in this experiment.

371 To evaluate the reliability of our measurements across different run combinations, we
372 performed an Intraclass Correlation Coefficient (ICC) analysis. The ICC is a widely used
373 reliability index that quantifies both the degree of correlation and agreement among repeated
374 measurements. We aimed to determine the minimal number of runs necessary to achieve reliability
375 comparable to our gold-standard while minimizing time and financial costs associated with data
376 collection. Our gold-standard for reliability was defined as the ICC value obtained by averaging
377 across three identical pairs of runs, which represents the highest achievable level of consistency
378 we could obtain from the data collected and serves as the benchmark against which all other run
379 combinations were compared. To this end, we calculated ICC values for a range of different run
380 combinations, including: one individual run, two individual runs, three individual runs, four
381 individual runs, five individual runs, six individual runs, one identical pair of runs and two identical
382 pairs of runs (Table 1). Individual runs refer to runs processed independently to generate unique
383 sets of CSF parameters, which are then averaged to assess reliability. In contrast, pairs of identical
384 runs involve averaging the timeseries of sets of runs with the same stimuli before processing to
385 yield a single set of CSF parameters for each pair.

386 To determine acceptable reliability, we selected an ICC threshold of 0.5 (Koo & Li, 2016;
387 Liljequist, Elfving, & Skavberg Roaldsen, 2019). An ICC value below 0.5 was considered to
388 indicate poor reliability. The aim was to determine which of these combinations could achieve
389 reliability equivalent to or greater than our gold-standard, thereby providing a reliable measure
390 while using the fewest possible runs.

391 A one-sample t-test was conducted to compare the ICC values of the eight different run
392 combinations against the threshold value of 0.5 across five parameters: peak contrast sensitivity,
393 peak spatial frequency, spatial frequency bandwidth, spatial frequency cutoff, and R² value. The
394 statistical significance of the results was evaluated using p-values, with Bonferroni correction
395 applied for multiple comparisons to control for Type I error. Run combinations with p-values
396 below 0.05 after correction were considered statistically significant.

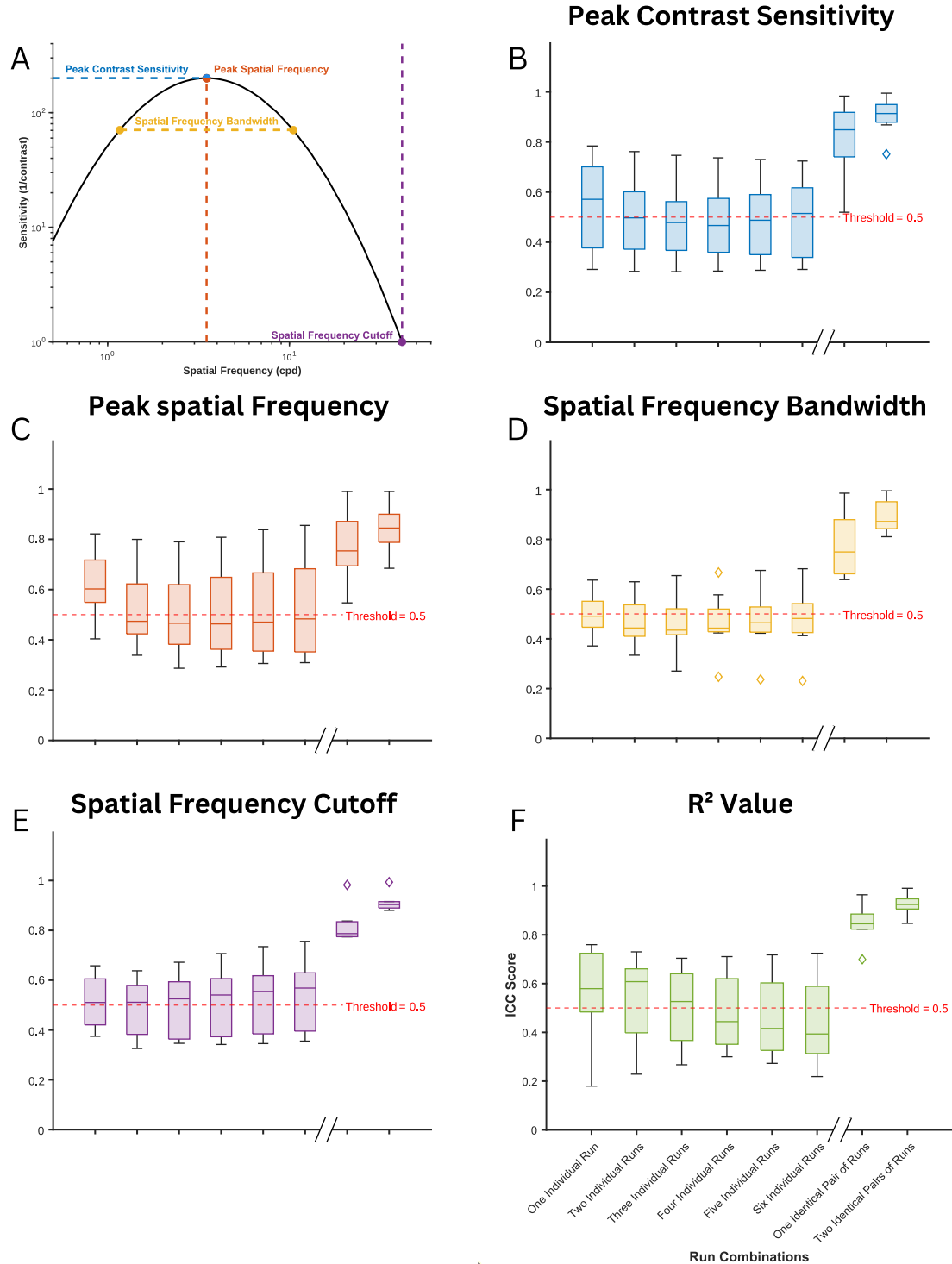
INDEX	RUN COMBINATIONS	RUNS INCLUDED
1		[1]
...	one individual run	...
6		[6]
7		[1,2]
...	two individual runs	...
21		[5,6]
22		[1,2,3]
...	three individual runs	...
41		[4,5,6]
42		[1,2,3,4]
...	four individual runs	...
56		[3,4,5,6]
57		[1,2,3,4,5]
...	five individual runs	...
62		[2,3,4,5,6]
63		[1,2,3,4,5,6]
64		[1&4]
65	one identical pair of runs	[2&5]
66		[3&6]
67		[1&4, 2&5]
68	two identical pairs of runs	[1&4, 3&6]
69		[2&5, 3&6]

397 **Table 1. Short List of the 69 Run Combinations Included in the Intraclass Correlation Coefficient (ICC) Analysis.** The table
398 details a selection of the combinations of runs used in the ICC analysis, organized by the number of runs included: from single
399 individual runs to multiple individual runs, as well as pairs of identical runs that were averaged together. The symbol "," denotes
400 combinations of runs whose time series were individually processed to generate separate sets of contrast sensitivity function (CSF)
401 parameters, which were then averaged. The symbol "&" represents combinations of runs with identical sets of stimuli, where the
402 time series were averaged prior to processing to yield a single set of CSF parameters.

403 Out of the eight combinations tested, only "one identical pair of runs" and "two identical
404 pairs of runs" achieved reliability greater than our threshold value (Fig. 10). The results were
405 similar across all parameters. For "one identical pair of runs," significant results were found for
406 peak contrast sensitivity ($t(7) = 5.870$, $p < 0.01$), peak spatial frequency ($t(7) = 5.513$, $p < 0.01$),
407 spatial frequency bandwidth ($t(7) = 6.075$, $p < 0.01$), spatial frequency cutoff ($t(7) = 12.703$, $p <$
408 0.001), and R^2 value ($t(7) = 12.970$, $p < 0.001$). The "two identical pairs of runs" also showed
409 significant results for peak contrast sensitivity ($t(7) = 15.581$, $p < 0.001$), peak spatial frequency
410 ($t(7) = 10.051$, $p < 0.001$), spatial frequency bandwidth ($t(7) = 16.371$, $p < 0.001$), spatial frequency
411 cutoff ($t(7) = 32.722$, $p < 0.001$), and R^2 value ($t(7) = 27.398$, $p < 0.001$). None of the other run
412 combinations yielded results that were above the threshold across any of the parameters tested (all
413 $p > 0.05$). These findings suggest that it is possible to reduce the number of runs and still maintain
414 robust data quality, offering a more efficient and economical approach to data collection.

415 **4. Discussion**

416 The neuroCSF is a novel fMRI model-driven approach that combines dynamic stimulation,
417 with a canonical model of the CSF and parameter optimization to provide voxel- wise CSF
418 estimations across early visual areas. With this new method, we were able to derive robust and
419 interpretable estimates of cortical CSF parameters to provide the first complete characterization of
420 the CSF using neuroimaging data. Our approach provides estimates of four parameters per visual
421 field location: peak gain, peak spatial frequency, spatial frequency bandwidth, and the cut-off
422 frequency of the CSF.



423

424 **Figure 10. Distribution of Intraclass Correlation Coefficient (ICC) values for all combinations of runs compared to the gold**
 425 **standard across five CSF parameters.** (A) The Contrast Sensitivity Function (CSF) curve with markers indicating the four
 426 parameters: peak contrast sensitivity (blue), peak spatial frequency (red), spatial frequency bandwidth (orange), and spatial
 427 frequency cutoff (purple). (B-F) ICC values across different run combinations for each parameter: (B) Peak Contrast Sensitivity, (C)
 428 Peak Spatial Frequency, (D) Spatial Frequency Bandwidth, (E) Spatial Frequency Cutoff, and (F) R^2 Value. The horizontal red dashed
 429 line at $\text{ICC} = 0.5$ indicates the threshold for acceptable reliability. Asterisks (*) denote run combinations that are statistically
 430 significantly different from the threshold ($\text{ICC score} = 0.5$).

431 One of the major concerns of vision neuroscience is to relate the organization of cortical
432 processing to perception. Psychophysical studies have consistently shown that behavioral
433 measures of contrast and spatial frequency sensitivities decrease from foveal to peripheral
434 eccentricities. Previous neuroimaging and neurophysiological studies independently estimated
435 human spatial frequency tuning (Aghajari et al., 2020; Broderick et al., 2022; Henriksson et al.,
436 2008; Singh, Smith, & Greenlee, 2000; Sirovich & Uglesich, 2004) and contrast sensitivity
437 (Himmelberg & Wade, 2019; Marquardt, Schneider, Gulban, Ivanov, & Uludağ, 2018) across the
438 visual cortex. To our knowledge, the neuroCSF is the first human neuroimaging approach that
439 unifies these measurements. This integration allowed us to explore the spatial organization of the
440 CSF across early visual areas to provide valuable insights into the relationship between behavioral
441 CSF measurements and their cortical counterparts.

442 The dependency of CSF parameters on retinotopy and eccentricity that we found in all
443 three visual areas was consistent with prior studies (Aghajari et al., 2020; Broderick et al., 2022;
444 Campbell, Cooper, & Enroth-Cugell, 1969; De Valois et al., 1982; Foster et al., 1985; Movshon,
445 Thompson, & Tolhurst, 1978). Our results support Aghajari et al. (2020); Campbell et al. (1969);
446 Movshon et al. (1978) findings, suggesting a fast rate of peak spatial frequency decline with
447 eccentricity across V1-V3. Similarly to Henriksson et al. (2008), V2 voxels optimal spatial
448 frequencies were on average 2/3 of the peak spatial frequency in V1. We also observed a similar
449 shift from V2 to V3. Spatial frequency bandwidth changes with eccentricity were similar across
450 V1&V3, with larger values in peripheral eccentricity. Spatial frequency bandwidth remained
451 relatively consistent across eccentricity for V2. These results match previous conflicting reports
452 of the relationship between spatial frequency selectivity and eccentricity (Aghajari et al., 2020;
453 Broderick et al., 2022; De Valois et al., 1982; Foster et al., 1985). Aghajari et al. (2020) noted a

454 slight increase in bandwidth with eccentricity but only for the perifovea. Since we only sampled
455 the fovea and parafovea this could explain why we didn't detect a similar trend between spatial
456 frequency selectivity and eccentricity. These results can help resolve some of the discrepancies in
457 the literature regarding spatial frequency selectivity and eccentricity.

458 Peak gain was found to be independent of eccentricity across V1-V3. By using full field
459 stimuli, we ensured the cortical representation of the gratings at various eccentricities became
460 equal in size, compensating for the reduced cortical representation that usually limits contrast
461 sensitivity in the periphery (Himmelberg et al., 2020; Horton & Hoyt, 1991; Rovamo & Virsu,
462 1979; Rovamo et al., 1978; Virsu & Rovamo, 1979). Similarly to Broderick et al. (2022), our
463 results did not reveal a significant trend between spatial frequency cutoff and eccentricity for area
464 V1. When looking at the individual CSFs (Fig. 9a), we can also see that for some subjects (S03,
465 S06, S08), the parafoveal spatial frequency cutoff was higher than the foveal one. These results
466 could be explained by the variability in foveal size that exists across the population (Noah C.
467 Benson et al., 2022; Henriksson, Karvonen, Salminen-Vaparanta, Railo, & Vanni, 2012; Schira,
468 Tyler, Breakspear, & Spehar, 2009). Our estimates of retinal location were obtained from a
469 probabilistic atlas (N. C. Benson et al., 2012) based on cortical-anatomical landmarks averaged
470 across 25 individuals. Noah C. Benson et al. (2022) showed that the use of automated anatomical
471 templates was less effective at estimating spatial layout of the visual field than mapping the
472 retinotopic organization. They showed a two-fold variation in amount of cortex devoted to the
473 fovea across individuals. This suggests that standardized atlases may not capture the true extent of
474 variability found in individuals retinotopic maps, and hence mistakenly label parafoveal voxels as
475 foveal ones and vice-versa. These results could also explain why we did not find a statistically

476 significant difference between fovea and parafovea spatial frequency cutoffs in V1. However, we
477 did find a significant effect of eccentricity on the cutoff for V2-V3 voxels.

478 In comparison with behavioral measures, the neuroCSF CSF curves were of similar shapes,
479 but they were shifted along the x-axis toward lower spatial frequencies. When measured
480 psychophysically, both human and macaque contrast sensitivity tends to peak between 3-5 (cpd)
481 (De Valois, Morgan, & Snodderly, 1974; Watson & Ahumada, 2005), and these values shift toward
482 lower frequencies with increasing eccentricity. Our results indicated an overall lower resolution of
483 early visual areas voxels with mean foveal spatial frequency optima of 1.9 cpd, 1.7 cpd and 1.6
484 cpd for V1, V2 and V3 respectively. Comparison between cortical and behavioral results is not
485 straightforward and several factors inherent to the differences between fMRI and psychophysical
486 measurements of visual function could explain these discrepancies.

487 NeuroCSF directly measures cortical sensitivity in relation to visual stimuli, capturing
488 neural processing in early visual cortex. This cortical activity might not have a one-to-one
489 correspondence to perceived sensitivity. Behavioral CSF involves higher-level visual processing
490 and cognitive compensations such as attention (Gandhi, Heeger, & Boynton, 1999; Ress, Backus,
491 & Heeger, 2000; Ress & Heeger, 2003) and decision-making processes (e.g., learning, experience,
492 and cognitive strategies), potentially shifting sensitivity. These cognitive processes can integrate
493 information over time and space, which may lead to increased sensitivity, especially at higher
494 spatial frequencies. Uncertainty related to the precise timing and perception of our stimulus might
495 have also influenced cortical activity level. Subjects were presented with a low-contrast target that
496 was sometimes reported as “hard to perceive” and they were allowed to completely disengage their
497 attention during the interstimulus intervals. Ress et al. (2000) showed that fMRI measurements of
498 cortical activity in early visual areas during a contrast detection task highly depend on attention-

499 related signals. Our low sensitivity results might therefore be a consequence of low visual
500 attention.

501 fMRI inherently has limitations in spatial resolution, and the neuroCSF results are
502 contingent on the spatial precision of the imaging. Fine-grained CSF changes may be challenging
503 to detect due to the limited spatial resolution of fMRI. This limitation can potentially lead to
504 underestimations or misinterpretations of CSF parameters, especially when investigating subtle
505 changes in visual perception. A large voxel size may result in spatial averaging of neural responses,
506 potentially leading to a shift in the peak spatial frequency toward lower values. Therefore, careful
507 consideration of spatial resolution constraints is crucial.

508 Our approach differs from existing methods to measure human CSF in that it overcomes
509 measurement trade-offs and patient limitations, while also presenting pathophysiological
510 relevance. Traditional approaches to measuring the human CSF face trade-offs between precision
511 and testing time, limiting their utility. When sampling the two-dimensional space of possible
512 stimuli- defined by contrast and spatial frequency- the range of stimuli needs to be wide enough
513 to capture the global shape of the CSF, but it also needs to be precise enough to capture the highly
514 dynamic regions of the curve such as the high-frequency cutoff. To improve the flexibility and
515 precision of traditional CSF tests, sampling range needs to be increased, but this would introduce
516 the cost of extra testing time. In contrast, with our model-driven approach that is combined with
517 dynamic stimuli, we can sweep through a wide range of spatial frequency and contrast across the
518 visual field over a short period of time. This strategy allows for a wide sampling range and
519 resolution without increased testing time.

520 Current methods to measure the CSF can be challenging for healthy participants, and even
521 more so for patients who suffer from attention or fixation problems and visual discomfort (Kalia

522 et al., 2014; Lesmes et al., 2010). These factors can also influence the reliability of current
523 behavioral CSF measures (Abrahamyan et al., 2016; Abramov et al., 1984; Bradley & Freeman,
524 1982; Lee et al., 2014). With its use of a full field stimuli, neuroCSF eliminates the need for
525 participant fixation. Our novel technique also estimates the CSF without the need for participant
526 input, making it suitable for nonverbal individuals like infants or those with intellectual disabilities.

527 While neuroCSF offers advantages in stimulus flexibility, optimizing stimulus designs to
528 accurately capture the complete CSF profile is not without challenges. Balancing the range and
529 resolution of stimuli while minimizing testing time remains a methodological concern that needs
530 careful consideration. Next iterations of the stimulus could be more targeted to reduce the scanning
531 time. We are currently working on an optimization approach to define a set of stimuli that yields
532 the most information about the CSF's overall shape.

533 The use of ICC analysis helped us identify the optimal number and types of runs required
534 to achieve high reliability with neuroCSF measurements. The results suggest that while the use of
535 a single or multiple individual runs often yields moderate ICC values (i.e., below the threshold of
536 0.5), combining identical runs before data processing significantly enhances reliability, exceeding
537 the 0.5 threshold for ICC scores in all cases. By identifying combinations of runs that can achieve
538 reliable measurements with fewer repetitions, our analysis offers a practical framework for
539 optimizing data collection. This has important implications for future studies, where minimizing
540 participant burden and resource usage is crucial.

541 Although the neuroCSF technique provides valuable insights into cortical CSF parameters,
542 its relationship to traditional behavioral CSF measures should be further validated. Understanding
543 the degree of correspondence between neuroimaging-derived CSF estimates and psychophysical
544 measurements is crucial for establishing its reliability and validity.

545 The neuroCSF technique relies on a log-parabolic model to describe CSF parameters. This
546 model of the CSF is a simplified version of the truncated log-parabola that has previously been
547 used in psychophysical studies to estimate CSF parameters (Lesmes et al., 2010; Rosenkranz et
548 al., 2021; Tardif, Watson, Giaschi, & Gosselin, 2021; Watson & Ahumada, 2005), and has been
549 shown to provide, compared to other models, excellent fits with very few assumptions, parameters
550 and calculations (Gao et al., 2015; Reynaud, Tang, Zhou, & Hess, 2014; Spiegel et al., 2016;
551 Watson & Ahumada, 2005). While this model simplifies the estimation process, it may not fully
552 capture all the nuances of individual differences or variations in CSF profiles. The symmetric log-
553 parabola typically misfits the plateau observed on the peak's low-frequency side (Rohaly &
554 Owsley, 1993). This could constrain the model's accuracy in specific cases. With an additional
555 parameter to describe the low-frequency plateau, the truncated log-parabola can deal with the
556 issues of the CSF's asymmetry.

557 Addressing these limitations and conducting further research to mitigate their impact will
558 be essential for harnessing the full potential of the neuroCSF technique.

559 5. Data and Code Availability

560 The data that support the findings of this study are available on request from the
561 corresponding author.

562 6. Authors Contributions

563 **Laurie Goulet:** Conceptualization, Methodology, Software, Formal analysis,
564 Investigation, Writing – Original Draft, Visualization. **Reza Farivar:** Conceptualization,
565 Methodology, Resources, Writing – Review & Editing, Project administration, Funding
566 acquisition.

567 7. Acknowledgements

568 This research was partly supported by CIHR under Grant Number 899956. The authors
569 declare no competing interests.

570 8. References

- 571 Ab Wahab, M. N., Nefti-Meziani, S., & Atyabi, A. (2015). A comprehensive review of swarm
572 optimization algorithms. *PLoS One*, 10(5), e0122827. doi:10.1371/journal.pone.0122827
- 573 Abrahamyan, A., Silva, L. L., Dakin, S. C., Carandini, M., & Gardner, J. L. (2016). Adaptable
574 history biases in human perceptual decisions. *Proceedings of the National Academy of
575 Sciences*, 113(25), E3548-E3557. doi:10.1073/pnas.1518786113
- 576 Abramov, I., Hainline, L., Turkel, J., Lemire, E., Smith, H., Gordon, J., & Petry, S. (1984).
577 Rocket-ship psychophysics. Assessing visual functioning in young children. *Invest
578 Ophthalmol Vis Sci*, 25(11), 1307-1315.
- 579 Aghajari, S., Vinke, L. N., & Ling, S. (2020). Population spatial frequency tuning in human early
580 visual cortex. *Journal of Neurophysiology*, 123(2), 773-785. doi:10.1152/jn.00291.2019
- 581 Alvarez, I., De Haas, B., Clark, C., Rees, G., & Schwarzkopf, D. (2015). Comparing different
582 stimulus configurations for population receptive field mapping in human fMRI. *Frontiers
583 in Human Neuroscience*, 9(96). doi:10.3389/fnhum.2015.00096
- 584 Arden, G. B. (1978). The importance of measuring contrast sensitivity in cases of visual
585 disturbance. *British Journal of Ophthalmology*, 62(4), 198-209. doi:10.1136/bjo.62.4.198
- 586 Benson, N. C., Butt, O. H., Datta, R., Radoeva, P. D., Brainard, D. H., & Aguirre, G. K. (2012).
587 The Retinotopic Organization of Striate Cortex Is Well Predicted by Surface Topology.
588 *Current Biology*, 22(21), 2081-2085. doi:<https://doi.org/10.1016/j.cub.2012.09.014>
- 589 Benson, N. C., Yoon, J. M. D., Forenzo, D., Engel, S. A., Kay, K. N., & Winawer, J. (2022).
590 Variability of the Surface Area of the V1, V2, and V3 Maps in a Large Sample of Human
591 Observers. *The Journal of Neuroscience*, 42(46), 8629-8646. doi:10.1523/jneurosci.0690-
592 21.2022
- 593 Bradley, A., & Freeman, R. D. (1982). Contrast sensitivity in children. *Vision Research*, 22(8),
594 953-959. doi:[https://doi.org/10.1016/0042-6989\(82\)90031-1](https://doi.org/10.1016/0042-6989(82)90031-1)
- 595 Brainard, D. H. (1997). The Psychophysics Toolbox. *Spat Vis*, 10(4), 433-436.
- 596 Broderick, W. F., Simoncelli, E. P., & Winawer, J. (2022). Mapping spatial frequency preferences
597 across human primary visual cortex. *Journal of Vision*, 22(4), 3-3. doi:10.1167/jov.22.4.3
- 598 Campbell, F. W., Cooper, G. F., & Enroth-Cugell, C. (1969). The spatial selectivity of the visual
599 cells of the cat. *The Journal of physiology*, 203(1), 223-235.
600 doi:10.1113/jphysiol.1969.sp008861
- 601 Campbell, F. W., & Robson, J. G. (1968). Application of Fourier analysis to the visibility of
602 gratings. *J Physiol*, 197(3), 551-566. doi:10.1113/jphysiol.1968.sp008574
- 603 Cascairo, M. A., Mazow, M. L., Holladay, J., & Prager, T. (1997). Contrast visual acuity in treated
604 amblyopia. *Binocular Vision And Strabismus Quarterly*, 12, 167-174.
- 605 Chatzistefanou, K. I., Theodossiadis, G. P., Damanakis, A. G., Ladas, I. D., Moschos, M. N., &
606 Chimonidou, E. (2005). Contrast sensitivity in amblyopia: the fellow eye of untreated and
607 successfully treated amblyopes. *J aapos*, 9(5), 468-474. doi:10.1016/j.jaapos.2005.05.002

- 608 Chen, L., & Gordon, L. K. (2005). Ocular manifestations of multiple sclerosis. *Current Opinion
609 in Ophthalmology*, 16(5), 315-320. doi:10.1097/01.icu.0000179804.49842.e2
- 610 Chung, S. T., & Legge, G. E. (2016). Comparing the Shape of Contrast Sensitivity Functions for
611 Normal and Low Vision. *Invest Ophthalmol Vis Sci*, 57(1), 198-207. doi:10.1167/iovs.15-
612 18084
- 613 Cocce, K. J., Stinnett, S. S., Luhmann, U. F. O., Vajzovic, L., Horne, A., Schuman, S. G., . . . Lad,
614 E. M. (2018). Visual Function Metrics in Early and Intermediate Dry Age-related Macular
615 Degeneration for Use as Clinical Trial Endpoints. *Am J Ophthalmol*, 189, 127-138.
616 doi:10.1016/j.ajo.2018.02.012
- 617 Collins, M. W., Kontos, A. P., Okonkwo, D. O., Almquist, J., Bailes, J., Barisa, M., . . . Zafonte,
618 R. (2016). Statements of Agreement From the Targeted Evaluation and Active
619 Management (TEAM) Approaches to Treating Concussion Meeting Held in Pittsburgh,
620 October 15-16, 2015. *Neurosurgery*, 79(6), 912-929. doi:10.1227/neu.0000000000001447
- 621 Cox, R. W. (1996). AFNI: software for analysis and visualization of functional magnetic resonance
622 neuroimages. *Comput Biomed Res*, 29(3), 162-173. doi:10.1006/cbmr.1996.0014
- 623 Dakin, S. C., & Turnbull, P. R. K. (2016). Similar contrast sensitivity functions measured using
624 psychophysics and optokinetic nystagmus. *Scientific Reports*, 6(1), 34514.
625 doi:10.1038/srep34514
- 626 De Valois, R. L., Albrecht, D. G., & Thorell, L. G. (1982). Spatial frequency selectivity of cells in
627 macaque visual cortex. *Vision Res*, 22(5), 545-559. doi:10.1016/0042-6989(82)90113-4
- 628 De Valois, R. L., Morgan, H., & Snodderly, D. M. (1974). Psychophysical studies of monkey
629 vision. 3. Spatial luminance contrast sensitivity tests of macaque and human observers.
630 *Vision Res*, 14(1), 75-81. doi:10.1016/0042-6989(74)90118-7
- 631 Farivar, R., Grigorov, F., van der Kouwe, A. J., Wald, L. L., & Keil, B. (2016). Dense, shape-
632 optimized posterior 32-channel coil for submillimeter functional imaging of visual cortex
633 at 3T. *Magn Reson Med*, 76(1), 321-328. doi:10.1002/mrm.25815
- 634 Foster, K. H., Gaska, J. P., Nagler, M., & Pollen, D. A. (1985). Spatial and temporal frequency
635 selectivity of neurones in visual cortical areas V1 and V2 of the macaque monkey. *The
636 Journal of physiology*, 365, 331-363. doi:10.1113/jphysiol.1985.sp015776
- 637 Gandhi, S. P., Heeger, D. J., & Boynton, G. M. (1999). Spatial attention affects brain activity in
638 human primary visual cortex. *Proc Natl Acad Sci U S A*, 96(6), 3314-3319.
639 doi:10.1073/pnas.96.6.3314
- 640 Gao, Y., Reynaud, A., Tang, Y., Feng, L., Zhou, Y., & Hess, R. F. (2015). The amblyopic deficit
641 for 2nd order processing: Generality and laterality. *Vision Research*, 114, 111-121.
642 doi:<https://doi.org/10.1016/j.visres.2014.10.020>
- 643 Gervais, M. J., Harvey, L. O., Jr., & Roberts, J. O. (1984). Identification confusions among letters
644 of the alphabet. *J Exp Psychol Hum Percept Perform*, 10(5), 655-666. doi:10.1037//0096-
645 1523.10.5.655
- 646 Harvey, L. O., Jr. (1997). Efficient estimation of sensory thresholds with ML-PEST. *Spat Vis*,
647 11(1), 121-128. doi:10.1163/156856897x00159
- 648 Helwig, S., Branke, J., & Mostaghim, S. M. (2013). Experimental Analysis of Bound Handling
649 Techniques in Particle Swarm Optimization. *IEEE Transactions on Evolutionary
650 Computation*, 17(2). doi:10.1109/TEVC.2012.2189404
- 651 Hemptinne, C., Liu-Shuang, J., Yuksel, D., & Rossion, B. (2018). Rapid Objective Assessment of
652 Contrast Sensitivity and Visual Acuity With Sweep Visual Evoked Potentials and an

- 653 Extended Electrode Array. *Investigative Ophthalmology & Visual Science*, 59(2), 1144-
654 1157. doi:10.1167/iovs.17-23248
- 655 Henriksson, L., Karvonen, J., Salminen-Vaparanta, N., Railo, H., & Vanni, S. (2012). Retinotopic
656 Maps, Spatial Tuning, and Locations of Human Visual Areas in Surface Coordinates
657 Characterized with Multifocal and Blocked fMRI Designs. *PLoS One*, 7(5), e36859.
658 doi:10.1371/journal.pone.0036859
- 659 Henriksson, L., Nurminen, L., Hyvärinen, A., & Vanni, S. (2008). Spatial frequency tuning in
660 human retinotopic visual areas. *Journal of Vision*, 8(10), 5-5. doi:10.1167/8.10.5
- 661 Hess, R. F., Li, X., Mansouri, B., Thompson, B., & Hansen, B. C. (2009). Selectivity as well as
662 sensitivity loss characterizes the cortical spatial frequency deficit in amblyopia. *Hum Brain
663 Mapp*, 30(12), 4054-4069. doi:10.1002/hbm.20829
- 664 Himmelberg, M. M., & Wade, A. R. (2019). Eccentricity-dependent temporal contrast tuning in
665 human visual cortex measured with fMRI. *NeuroImage*, 184, 462-474.
666 doi:<https://doi.org/10.1016/j.neuroimage.2018.09.049>
- 667 Himmelberg, M. M., Winawer, J., & Carrasco, M. (2020). Stimulus-dependent contrast sensitivity
668 asymmetries around the visual field. *Journal of Vision*, 20(9), 18-18.
669 doi:10.1167/jov.20.9.18
- 670 Hoffmann, L., Rossouw, P., Guichard, M. M., & Hatz, K. (2020). Strongest Correlation Between
671 Contrast Sensitivity and Morphological Characteristics in Bilateral nAMD. *Front Med
672 (Lausanne)*, 7, 622877. doi:10.3389/fmed.2020.622877
- 673 Horton, J. C., & Hoyt, W. F. (1991). The Representation of the Visual Field in Human Striate
674 Cortex: A Revision of the Classic Holmes Map. *Archives of Ophthalmology*, 109(6), 816-
675 824. doi:10.1001/archopht.1991.01080060080030
- 676 Howe, J. W., & Mitchell, K. W. (1984). The objective assessment of contrast sensitivity function
677 by electrophysiological means. *British Journal of Ophthalmology*, 68(9), 626-638.
678 doi:10.1136/bjo.68.9.626
- 679 Huang, C., Tao, L., Zhou, Y., & Lu, Z. L. (2007). Treated amblyopes remain deficient in spatial
680 vision: a contrast sensitivity and external noise study. *Vision Res*, 47(1), 22-34.
681 doi:10.1016/j.visres.2006.09.015
- 682 Jackson, T. L., Ong, G. L., & Ripley, L. G. (2004). Orientational contrast sensitivity and chromatic
683 contrast thresholds in multiple sclerosis. *Am J Ophthalmol*, 137(2), 283-286.
684 doi:10.1016/j.ajo.2003.08.032
- 685 Jindra, L. F., & Zemon, V. (1989). Contrast sensitivity testing: A more complete assessment of
686 vision. *Journal of Cataract & Refractive Surgery*, 15(2), 141-148.
687 doi:[https://doi.org/10.1016/S0886-3350\(89\)80002-1](https://doi.org/10.1016/S0886-3350(89)80002-1)
- 688 Jones, P. R., Kalwarowsky, S., Atkinson, J., Braddick, O. J., & Nardini, M. (2014). Automated
689 Measurement of Resolution Acuity in Infants Using Remote Eye-Tracking. *Investigative
690 Ophthalmology & Visual Science*, 55(12), 8102-8110. doi:10.1167/iovs.14-15108
- 691 Kalia, A., Lesmes, L. A., Dorr, M., Gandhi, T., Chatterjee, G., Ganesh, S., . . . Sinha, P. (2014).
692 Development of pattern vision following early and extended blindness. *Proceedings of the
693 National Academy of Sciences*, 111(5), 2035-2039. doi:doi:10.1073/pnas.1311041111
- 694 Katz, L. M., Levi, D. M., & Bedell, H. E. (1984). Central and peripheral contrast sensitivity in
695 amblyopia with varying field size. *Doc Ophthalmol*, 58(4), 351-373.
696 doi:10.1007/bf00679799

- 697 Kelly, D. H., & Savoie, R. E. (1973). A study of sine-wave contrast sensitivity by two
698 psychophysical methods. *Perception & Psychophysics*, 14(2), 313-318.
699 doi:10.3758/BF03212397
- 700 Klein, R., Wang, Q., Klein, B. E., Moss, S. E., & Meuer, S. M. (1995). The relationship of age-
701 related maculopathy, cataract, and glaucoma to visual acuity. *Invest Ophthalmol Vis Sci*,
702 36(1), 182-191.
- 703 Kleiner, R. C., Enger, C., Alexander, M. F., & Fine, S. L. (1988). Contrast sensitivity in age-related
704 macular degeneration. *Arch Ophthalmol*, 106(1), 55-57.
705 doi:10.1001/archopht.1988.01060130061028
- 706 Koo, T. K., & Li, M. Y. (2016). A Guideline of Selecting and Reporting Intraclass Correlation
707 Coefficients for Reliability Research. *J Chiropr Med*, 15(2), 155-163.
708 doi:10.1016/j.jcm.2016.02.012
- 709 Lee, T. H., Baek, J., Lu, Z. L., & Mather, M. (2014). How arousal modulates the visual contrast
710 sensitivity function. *Emotion*, 14(5), 978-984. doi:10.1037/a0037047
- 711 Legge, G. E., Rubin, G. S., Pelli, D. G., & Schleske, M. M. (1985). Psychophysics of reading—II.
712 Low vision. *Vision Research*, 25(2), 253-265. doi:[https://doi.org/10.1016/0042-6989\(85\)90118-X](https://doi.org/10.1016/0042-6989(85)90118-X)
- 713 Lesmes, L. A., Lu, Z. L., Baek, J., & Albright, T. D. (2010). Bayesian adaptive estimation of the
714 contrast sensitivity function: the quick CSF method. *J Vis*, 10(3), 17.11-21.
715 doi:10.1167/10.3.17
- 716 Liljequist, D., Elfving, B., & Skavberg Roaldsen, K. (2019). Intraclass correlation - A discussion
717 and demonstration of basic features. *PLoS One*, 14(7), e0219854.
718 doi:10.1371/journal.pone.0219854
- 719 Lopes de Faria, J. M., Katsumi, O., Arai, M., & Hirose, T. (1998). Objective measurement of
720 contrast sensitivity function using contrast sweep visual evoked responses. *The British
721 journal of ophthalmology*, 82(2), 168-173. doi:10.1136/bjo.82.2.168
- 722 Lovie-Kitchin, J., Mainstone, J., Robinson, J., & Brown, B. (1990). What areas of the visual
723 field are important for mobility in low vision patients. *Clinical vision sciences*.
- 724 Marquardt, I., Schneider, M., Gulban, O. F., Ivanov, D., & Uludağ, K. (2018). Cortical depth
725 profiles of luminance contrast responses in human V1 and V2 using 7 T fMRI. *Hum Brain
726 Mapp*, 39(7), 2812-2827. doi:10.1002/hbm.24042
- 727 Marron, J. A., & Bailey, I. L. (1982). Visual factors and orientation-mobility performance. *Am J
728 Optom Physiol Opt*, 59(5), 413-426. doi:10.1097/00006324-198205000-00009
- 729 McDonald, W. I., & Barnes, D. (1992). The ocular manifestations of multiple sclerosis. 1.
730 Abnormalities of the afferent visual system. *J Neurol Neurosurg Psychiatry*, 55(9), 747-
731 752. doi:10.1136/jnnp.55.9.747
- 732 Mendes, R., Kennedy, J., & Neves, J. (2004). The fully informed particle swarm: simpler, maybe
733 better. *IEEE Transactions on Evolutionary Computation*, 8(3).
734 doi:10.1109/TEVC.2004.826074
- 735 Midena, E., & Pilotto, E. (2017). Microperimetry in age-related macular degeneration. *Eye*, 31(7),
736 985-994. doi:10.1038/eye.2017.34
- 737 Mooney, S. W. J., Alam, N. M., Hill, N. J., & Prusky, G. T. (2020). Gradiate: A radial sweep
738 approach to measuring detailed contrast sensitivity functions from eye movements. *Journal
739 of Vision*, 20(13), 17-17. doi:10.1167/jov.20.13.17
- 740

- 741 Movshon, J. A., Thompson, I. D., & Tolhurst, D. J. (1978). Spatial and temporal contrast
742 sensitivity of neurones in areas 17 and 18 of the cat's visual cortex. *The Journal of*
743 *physiology*, 283, 101-120. doi:10.1113/jphysiol.1978.sp012490
- 744 Nunes, A. F., Monteiro, P. M., & Vaz Pato, M. (2014). Influence of multiple sclerosis, age and
745 degree of disability, in the position of the contrast sensitivity curve peak. *Indian J*
746 *Ophthalmol*, 62(2), 180-185. doi:10.4103/0301-4738.116485
- 747 Owsley, C., Huisinagh, C., Clark, M. E., Jackson, G. R., & McGwin, G., Jr. (2016). Comparison of
748 Visual Function in Older Eyes in the Earliest Stages of Age-related Macular Degeneration
749 to Those in Normal Macular Health. *Curr Eye Res*, 41(2), 266-272.
750 doi:10.3109/02713683.2015.1011282
- 751 Owsley, C., & Sloane, M. E. (1987). Contrast sensitivity, acuity, and the perception of 'real-world'
752 targets. *Br J Ophthalmol*, 71(10), 791-796. doi:10.1136/bjo.71.10.791
- 753 Ress, D., Backus, B. T., & Heeger, D. J. (2000). Activity in primary visual cortex predicts
754 performance in a visual detection task. *Nature Neuroscience*, 3(9), 940-945.
755 doi:10.1038/78856
- 756 Ress, D., & Heeger, D. J. (2003). Neuronal correlates of perception in early visual cortex. *Nature*
757 *Neuroscience*, 6(4), 414-420. doi:10.1038/nn1024
- 758 Reynaud, A., Tang, Y., Zhou, Y., & Hess, R. F. (2014). A normative framework for the study of
759 second-order sensitivity in vision. *Journal of Vision*, 14(9), 3-3. doi:10.1167/14.9.3
- 760 Ripley, D. L., & Politzer, T. (2010). Vision disturbance after TBI. *NeuroRehabilitation*, 27(3),
761 215-216. doi:10.3233/nre-2010-0599
- 762 Rogers, G. L., Bremer, D. L., & Leguire, L. E. (1987). The Contrast Sensitivity Function and
763 Childhood Amblyopia: Reply. *American Journal of Ophthalmology*, 104(6), 672-673.
764 doi:[https://doi.org/10.1016/0002-9394\(87\)90194-2](https://doi.org/10.1016/0002-9394(87)90194-2)
- 765 Rohaly, A. M., & Owsley, C. (1993). Modeling the contrast-sensitivity functions of older adults.
766 *Journal of the Optical Society of America A*, 10(7), 1591-1599.
767 doi:10.1364/JOSAA.10.001591
- 768 Rosenkranz, S. C., Kaulen, B., Zimmermann, H. G., Bittner, A. K., Dorr, M., & Stellmann, J.-P.
769 (2021). Validation of Computer-Adaptive Contrast Sensitivity as a Tool to Assess Visual
770 Impairment in Multiple Sclerosis Patients. *Frontiers in Neuroscience*, 15.
771 doi:10.3389/fnins.2021.591302
- 772 Rovamo, J., Franssila, R., & Näsänen, R. (1992). Contrast sensitivity as a function of spatial
773 frequency, viewing distance and eccentricity with and without spatial noise. *Vision Res*,
774 32(4), 631-637. doi:10.1016/0042-6989(92)90179-m
- 775 Rovamo, J., & Virsu, V. (1979). An estimation and application of the human cortical magnification
776 factor. *Experimental Brain Research*, 37(3), 495-510. doi:10.1007/BF00236819
- 777 Rovamo, J., Virsu, V., & NÄSÄNEN, R. (1978). Cortical magnification factor predicts the photopic
778 contrast sensitivity of peripheral vision. *Nature*, 271(5640), 54-56. doi:10.1038/271054a0
- 779 Schira, M. M., Tyler, C. W., Breakspear, M., & Spehar, B. (2009). The Foveal Confluence in
780 Human Visual Cortex. *The Journal of Neuroscience*, 29(28), 9050-9058.
781 doi:10.1523/jneurosci.1760-09.2009
- 782 Singh, K. D., Smith, A. T., & Greenlee, M. W. (2000). Spatiotemporal Frequency and Direction
783 Sensitivities of Human Visual Areas Measured Using fMRI. *NeuroImage*, 12(5), 550-564.
784 doi:<https://doi.org/10.1006/nimg.2000.0642>

- 785 Sirovich, L., & Uglesich, R. (2004). The organization of orientation and spatial frequency in
786 primary visual cortex. *Proceedings of the National Academy of Sciences*, 101(48), 16941-
787 16946. doi:doi:10.1073/pnas.0407450101
- 788 Sjöstrand, J. (1981). Contrast sensitivity in children with strabismic and anisometropic amblyopia.
789 A study of the effect of treatment *Acta Ophthalmologica*, 59(1), 25-34.
790 doi:<https://doi.org/10.1111/j.1755-3768.1981.tb06706.x>
- 791 Spiegel, D. P., Reynaud, A., Ruiz, T., Laguë-Beauvais, M., Hess, R., & Farivar, R. (2016). First-
792 and second-order contrast sensitivity functions reveal disrupted visual processing
793 following mild traumatic brain injury. *Vision Res*, 122, 43-50.
794 doi:10.1016/j.visres.2016.03.004
- 795 Stalin, A., & Dalton, K. (2020). Relationship of Contrast Sensitivity Measured Using Quick
796 Contrast Sensitivity Function With Other Visual Functions in a Low Vision Population.
797 *Investigative Ophthalmology & Visual Science*, 61(6), 21-21. doi:10.1167/iovs.61.6.21
- 798 Tardif, J., Watson, M. R., Giaschi, D., & Gosselin, F. (2021). The Curve Visible on the Campbell-
799 Robson Chart Is Not the Contrast Sensitivity Function. *Frontiers in Neuroscience*, 15.
800 doi:10.3389/fnins.2021.626466
- 801 Thomas, J. (1978). Normal and amblyopic contrast sensitivity function in central and peripheral
802 retinas. *Invest Ophthalmol Vis Sci*, 17(8), 746-753.
- 803 Virsu, V., & Rovamo, J. (1979). Visual resolution, contrast sensitivity, and the cortical
804 magnification factor. *Experimental Brain Research*, 37(3), 475-494.
805 doi:10.1007/BF00236818
- 806 Vision, N. R. C. C. o. (1985). In *Emergent Techniques for Assessment of Visual Performance*.
807 Washington (DC): National Academies Press (US)
- 808 Copyright © National Academy of Sciences.
- 809 Wang, G., Zhao, C., Ding, Q., & Wang, P. (2017). An Assessment of the Contrast Sensitivity in
810 Patients with Ametropic and Anisometropic Amblyopia in Achieving the Corrected Visual
811 Acuity of 1.0. *Scientific Reports*, 7(1), 42043. doi:10.1038/srep42043
- 812 Watson, A. B., & Ahumada, A. J., Jr. (2005). A standard model for foveal detection of spatial
813 contrast. *Journal of Vision*, 5(9), 6-6. doi:10.1167/5.9.6
- 814 West, S. K., Rubin, G. S., Broman, A. T., Muñoz, B., Bandeen-Roche, K., & Turano, K. (2002).
815 How does visual impairment affect performance on tasks of everyday life? The SEE
816 Project. Salisbury Eye Evaluation. *Arch Ophthalmol*, 120(6), 774-780.
817 doi:10.1001/archopht.120.6.774
- 818 Wong, W. L., Su, X., Li, X., Cheung, C. M., Klein, R., Cheng, C. Y., & Wong, T. Y. (2014).
819 Global prevalence of age-related macular degeneration and disease burden projection for
820 2020 and 2040: a systematic review and meta-analysis. *Lancet Glob Health*, 2(2), e106-
821 116. doi:10.1016/s2214-109x(13)70145-1
- 822 Woods, R. L., & Wood, J. M. (1995). The role of contrast sensitivity charts and contrast letter
823 charts in clinical practice. *Clinical and Experimental Optometry*, 78(2), 43-57.
824 doi:<https://doi.org/10.1111/j.1444-0938.1995.tb00787.x>
- 825 Worsley, K. J., Liao, C. H., Aston, J., Petre, V., Duncan, G. H., Morales, F., & Evans, A. C. (2002).
826 A general statistical analysis for fMRI data. *NeuroImage*, 15(1), 1-15.
827 doi:10.1006/nimg.2001.0933
- 828